ORNL/TM-2024/3558

NSUF BOILER Pre-Irradiation Characterization and High Flux Isotope Reactor Experiment Design

Nick Russell
Yukinori Yamamoto
Zain Karriem
Jose Salcedo Perez
Kory Linton
Tim Graening
Timothy Lach
Bruce Pint
Janelle Wharry

September 2024

OAK RIDGE National Laboratory

ORNL IS MANAGED BY UT-BATTELLE LLC FOR THE US DEPARTMENT OF ENERGY

ORNL/TM-2024/3558

Nuclear Energy and Fuel Cycle Division

NSUF BOILER PRE-IRRADIATION CHARACTERIZATION AND HIGH FLUX ISOTOPE REACTOR EXPERIMENT DESIGN

Nick Russell
Yukinori Yamamoto
Zain Karriem
Jose Salcedo Perez
Kory Linton
Tim Graening
Timothy Lach
Bruce Pint
Janelle Wharry

DOE-NE Nuclear Science User Facility (NSUF)
Milestone M3UA-23OR0102012

September 2024

Prepared by
OAK RIDGE NATIONAL LABORATORY
Oak Ridge, TN 37831
managed by
UT-BATTELLE LLC
for the
US DEPARTMENT OF ENERGY
under contract DE-AC05-00OR22725

CONTENTS

LIST OF FIGURES

ACKNOWLEDGMENTS

This research is supported by the US Department of Energy (DOE), Office of Nuclear Energy, Nuclear Science User Facilities (NSUF) program. The specimen alloys referenced in this report were fabricated in support of the Advanced Fuels Campaign within the Fuel Cycle Research and Development program, Office of Nuclear Energy. The report was authored by UT-Battelle under Contract No. DE-AC05-00OR22725 with the US DOE.

1. INTRODUCTION

Alumina-forming austenitic (AFA) stainless steels have emerged as a candidate alloy because of their high-temperature strength, formability, cost, and compatibility with primary coolants for lead-cooled fast reactors (LFRs). This class of steels has exceptional high-temperature oxidation performance; however, a high concentration of Ni is required to stabilize the austenite phase and to provide sufficient creep strength. AFA stainless steels are also susceptible to liquid metal embrittlement (LME). Additionally, under neutron irradiation, Ni will enrich at grain boundaries due to radiation-induced segregation (RIS). Nickel RIS can increase the LME under these coupled effects.

Oak Ridge National Laboratory (ORNL) and the NSUF program have leveraged its High Flux Isotope Reactor (HFIR) and experience with complex irradiation experiments to design experiment capsules that test the aforementioned coupled effects. These capsules are designed for insertion in the central flux trap, the highest flux region, of HFIR. The experiment capsules will be filled with Pb, designed to passively melt from the gamma heating in HFIR. The specimens were fabricated into miniature tensile specimens from two different alloys, GA05-25Ni and GA05-20Ni, varying Ni concentrations. The experiment capsules are designed to achieve target temperatures of 400 °C and 650 °C with accumulated dosage of 3 dpa.

This report documents the specimen alloy characterization, experimental design, and expected performance of the capsules.

2. SPECIMEN MATERIALS

2.1 MATERIAL CHARACTERIZATION AT UNIRRADIATED CONDITION

Two different AFA alloys, GA05-25Ni and GA05-20Ni, were prepared and evaluated in this project. The production of these alloys was supported in part by the Advanced Fuels Campaign within the Fuel Cycle Research and Development program, Office of Nuclear Energy. Nominally 43 kg of two columnar cast ingots with a size of 152 mm in diameter and 381 mm in length were prepared through vacuum induction melting with pure element feedstock by an external shop (Sophisticated Alloys, Inc., Butler, PA). The ingots were homogenized at 1149 °C for 3 h, hot-rolled at the same temperature targeting the plate thickness between 15.2 to 16.8 mm, and then annealed at 1149 °C for 30 min. Target and analyzed chemistry of the alloys can be found in Table 1.

Table 1. Target and analyzed alloy compositions of GA05-25Ni and -20Ni

Name	wt.%	Fe	Al	C	B	Cr	CU	Mn	Ni	Nb	Si	Ti	V	N	Remarks
GA05-25Ni	**Analyzed**	**Bal.**	**4.0**	**0.22**	**0.011**	**16.0**	**2.8**	**1.9**	**24.9**	**0.6**	**0.2**	**<0.01**	**<0.01**	**<0.01**	Heat #: 23086504-1
	Target	**48.99**	**4**	**0.2**	**0.01**	**16**	**3**	**2**	**25**	**0.6**	**0.2**	**0**	**0**	**0**	
	Max	Balance	4.2	0.22	0.015	16.5	3.5	2.5	25.5	0.8	0.5	0.05	0.05	0.02	
	Min	Balance	3.9	0.15	0.005	15.5	2.5	1.5	24.5	0.5	0.15				
GA05-20Ni	**Analyzed**	**Bal.**	**4.0**	**0.21**	**0.011**	**16.0**	**2.8**	**2.0**	**20.0**	**0.6**	**0.2**	**<0.01**	**<0.01**	**<0.01**	Heat #: 23086504-2
	Target	**53.99**	**4**	**0.2**	**0.01**	**16**	**3**	**2**	**20**	**0.6**	**0.2**	**0**	**0**	**0**	
	Max	Balance	4.2	0.22	0.015	16.5	3.5	2.5	20.5	0.8	0.5	0.05	0.05	0.02	
	Min	Balance	3.9	0.15	0.005	15.5	2.5	1.5	19.5	0.5	0.15				

Phase equilibrium of the alloys was calculated by a thermodynamic calculation software JMatPro v. 11 with the analyzed alloy compositions. The calculated phases of the alloys plotted as a function of temperature are shown in Figure 1. FCC-Fe with small amounts of primary MC (M: mainly Nb) and M_7C_3 (M: mainly Cr) are dominant at the process temperature (1149 °C), and secondary $M_{23}C_6$ (M: mainly Cr), B2-NiAL, Cu, and Sigma form mostly below 700 °C. No significant differences in the phases were observed between GA05-25Ni and -20Ni.

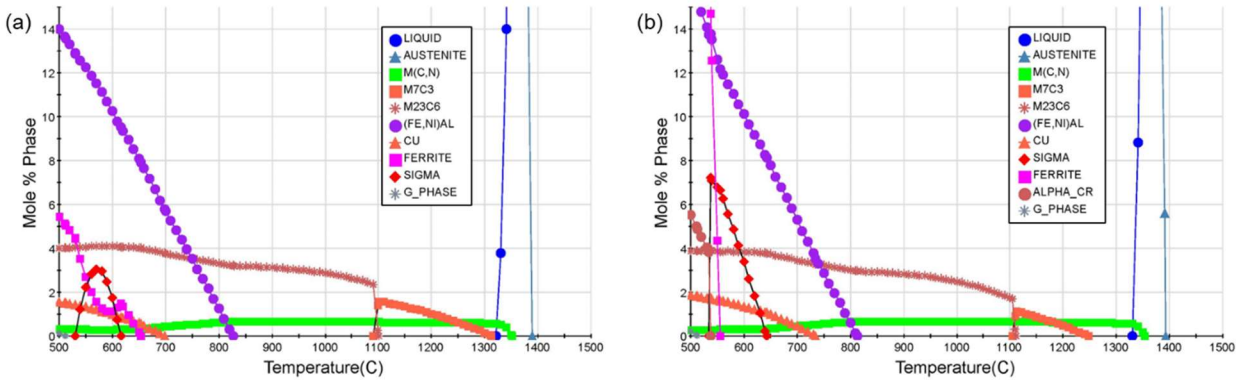

Figure 1. Calculated phase equilibrium of AFA alloys obtained from the analyzed alloy compositions. (a) GA05-25Ni and (b) GA05-20Ni.

The microstructure of the as-delivered plates was inhomogeneous in terms of primary NbC phase distribution and grain size variation, possibly due to an insufficient homogenization process; therefore, additional thermomechanical processes were applied at ORNL to obtain homogeneous microstructure.

The plates were re-homogenized at 1200 °C for 24 h in argon cover gas, cold-rolled with total 20% thickness reduction (targeting ~12.7 mm in thickness), and then annealed at 1149 °C for 30 min. Figure 2 shows the microstructures of the two alloys. The additional process resulted in relatively homogeneous primary NbC distribution as well as a uniform grain structure. The austenite grains are slightly elongated along the rolling direction (parallel to the horizontal axis in the micrographs) together with the aligned primary NbC particles on the grain boundaries. No clear evidence of M_7C_3 formation was found from the micrographs (note: M_7C_3 typically forms as coarse and blocky particles), although the detailed phase analysis has not yet been conducted. Both alloys showed grain sizes in the 30–100 μm range in most of the plate volume. It should be noted that coarse grains (>1 mm) still exist near the surface or the center of the plate thickness; thus, such areas were intentionally avoided for machining the tensile specimens (as described later).

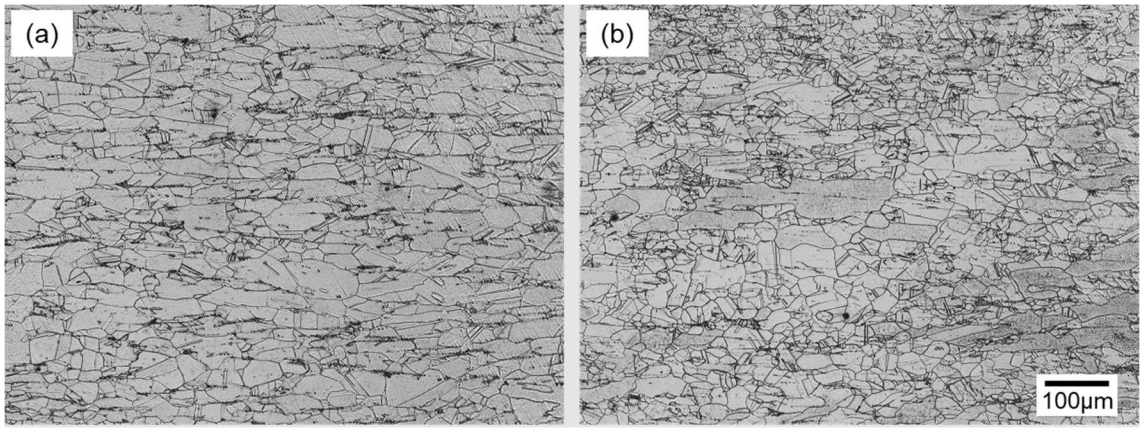

Figure 2. Optical micrographs of as-processed microstructure. (a) GA05-25Ni, and (b) GA05-20Ni.

Crystallographic orientation distribution was measured using a Quanta 650 FEG scanning electron microscope with electron backscatter diffraction (SEM-EBSD) equipped with an EDAX detector. The instrument was operated at 25 kV accelerating voltage, 2 μm step size, and 4x4 detector binning for data acquisition. Images were collected at different magnifications for the two alloys (350x for GA05-25Ni and 500x for GA05-20Ni) to show a consistent number of grains across the width of each collected map. Although the measured areas are relatively limited, both alloys showed no specific tendency (e.g., texture formation) on the orientation distribution, as shown in Figure 3. Further detailed characterization is currently in progress.

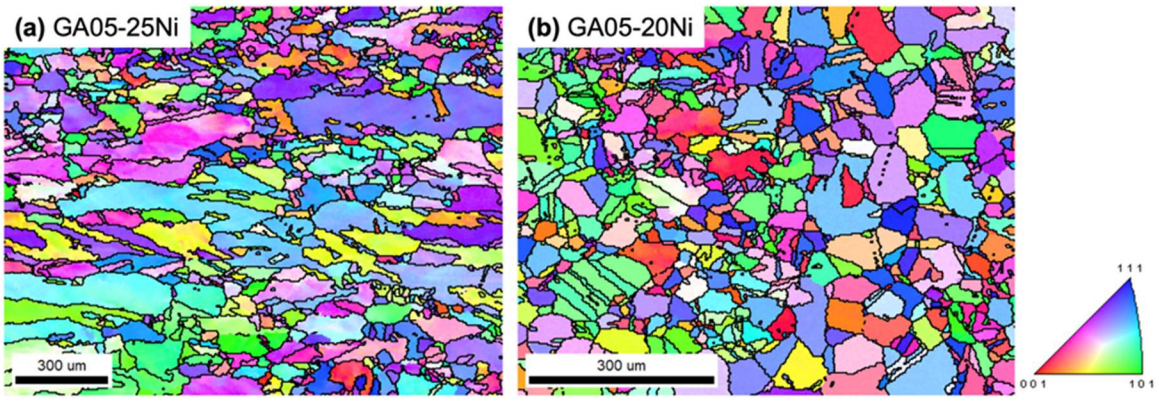

Figure 3. Inverse pole figure (IPF) color maps showing the crystallographic orientation of each grain acquired through SEM-EBSD analysis. (a) GA05-25Ni, and (b) GA05-20Ni.

Uniaxial tensile properties of both alloys were evaluated in the as-processed condition. Sub-sized dog-bone-shaped sheet tensile specimens (SS-3) were machined from the rolled-and-annealed plate with the tensile axis parallel to the rolling direction, as shown in Figure 4. The sectioning plan was proposed to avoid areas near the surface or the center of the plates where coarse austenite grains larger than 1 mm were present.

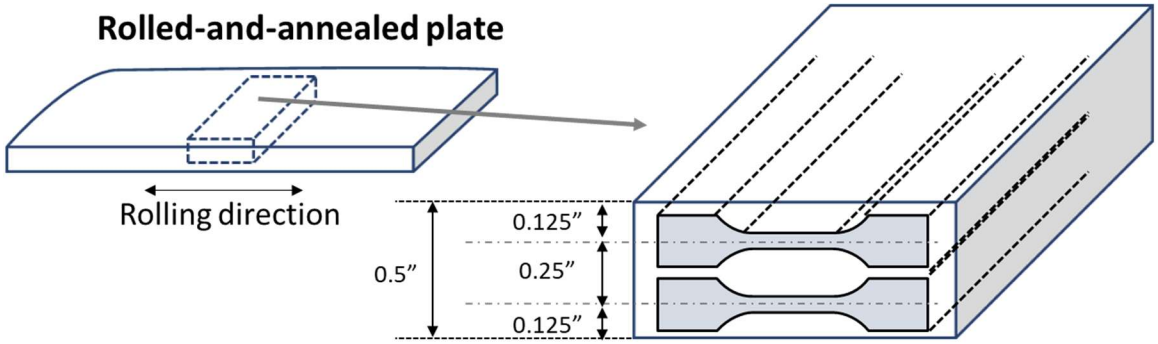

Figure 4. Sectioning plan of SS-3 specimens from the rolled-and-annealed plates.

The tensile tests were conducted in laboratory air at a constant crosshead speed targeting a strain rate of 1.0×10^{-3} s^{-1}. High temperature tests at 600, 700, and 800 °C were conducted with an induction heating system. The specimen temperature was directly measured by type K thermocouples attached to the specimen gauge. The tests were conducted after holding the specimens at the target temperature for no less than 10 min to make sure that the temperature was stabilized prior to the tests. Three tests were conducted at each test temperature, and the results are summarized with the averaged data.

The obtained tensile properties were plotted as a function of test temperature, as shown in Figure 5. The numerical data are also summarized in Table 2. In both alloys, the yield and ultimate tensile strength were mostly unchanged up to 600 °C and started decreasing above 700 °C. The ductility also dropped gradually up to 700 °C and then slightly recovered at 800 °C.

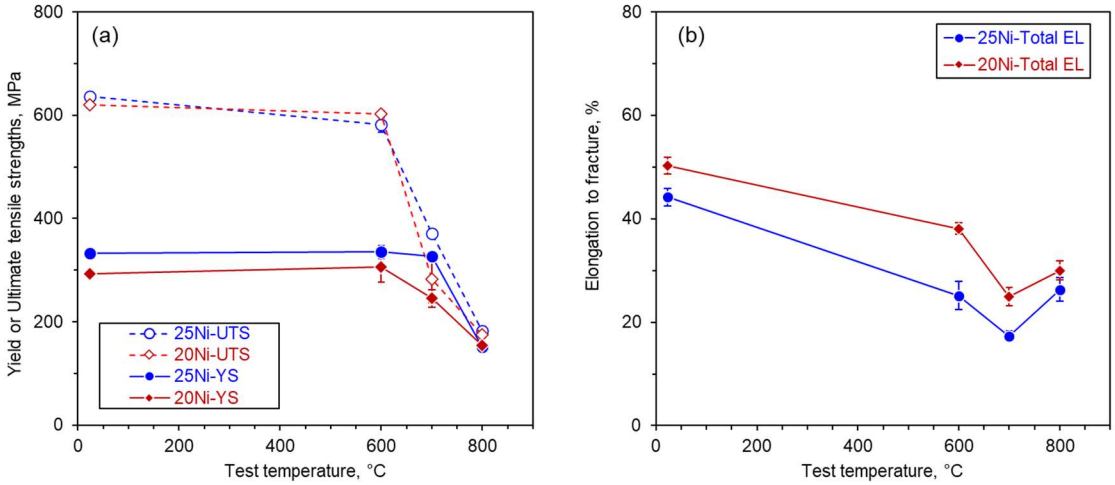

Figure 5. Uniaxial tensile properties of GA05-25Ni and -20Ni plotted as a function of test temperature.
(a) yield and ultimate tensile strength and (b) total plastic elongation.

Table 2. Uniaxial tensile properties: averaged three test results at each test condition

Alloy	Test temperature, °C	YS, MPa	UTS, MPa	Uniform plastic EL, %	Total plastic EL, %
GA05-25Ni	23	332 ± 3	637 ± 0	38 ± 1	44 ± 2
	600	335 ± 12	582 ± 15	234 ± 2	25 ± 3
	700	328 ± 5	371 ± 9	3 ± 0	17 ± 1
	800	152 ± 9	183 ± 9	3 ± 0	26 ± 2
GA05-20Ni	23	293 ± 6	621 ± 6	44 ± 2	50 ± 2
	600	307 ± 31	603 ± 5	35 ± 3	38 ± 1
	700	246 ± 17	283 ± 47	6 ± 3	25 ± 2
	800	154 ± 8	175 ± 5	5 ± 1	30 ± 2

2.2 SPECIMEN FABRICATION FOR IRRADIATION TESTING

In total, 60 of SS-J3 specimens (30 from GA05-25Ni and 30 from GA05-20Ni) were machined from the rolled-and-annealed plates. The sectioning plan is shown in Figure 6, which avoids areas near the surface and the center of the plates, just as the SS-J3 specimen machining approach shown in Figure 4. Pictures of as-delivered specimens are also shown in Figure 7. The specimens still require a pre-oxidation (2 h at 800 °C in air) to form external alumina-scale prior to the installation in the irradiation capsule [1].

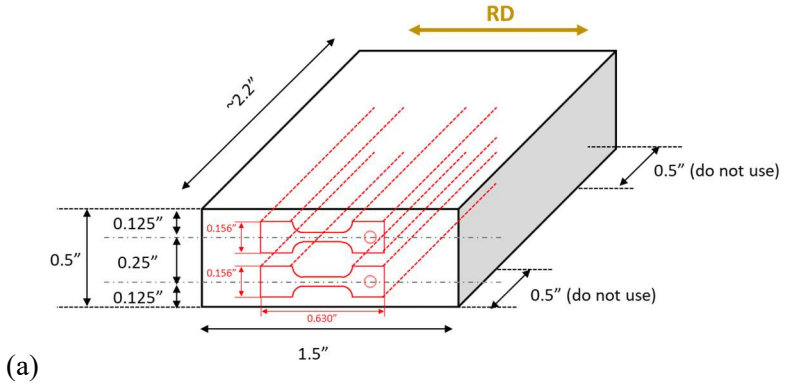

(a)

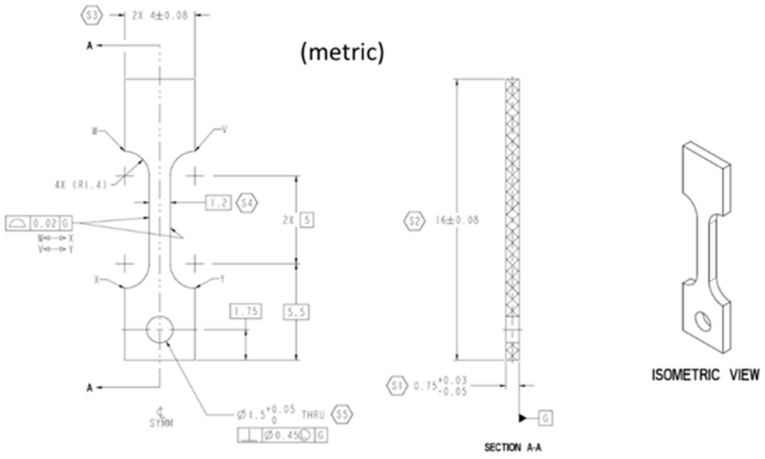

(b)

Figure 6. (a) Sectioning plan of SS-J3 specimens from the rolled-and-annealed plates and (b) drawing of SS-J3 specimens.

Figure 7. Fabricated SS-J3 miniature tensile specimens with 20% Ni alloy (G0 series) on left and 25% Ni alloy (G5 series) on right.

2.3 SPECIMEN MEASUREMENTS

Surface roughness measurements were performed using a Keyence VR series ONE-SHOT 3D microscope with the VR-5000 series software package (version 3.3.1.71). Both alloys were tested by placing 4 randomly selected SS-J3 tensile samples next to each other to investigate the reliability of measurements. The surface roughness could potentially have an impact on the wettability and corrosion performance of the material, which made it necessary to verify that the specimens show comparable values.

Testing of the surface roughness was performed on the tap section and the gauge section as area mapping measuring the *arithmetical mean height of the area* S_a and the *maximum height within the area* S_z. Additionally, 11 linescans across the gauge section were performed to measure the variability in the tensile test direction using the values *arithmetical mean height of the linescan* R_a and *maximum height within the linescan* R_z. The measured areas are shown in Figure 8, with 1 to 4 on the tap section, which will be used for the microstructure characterization, and area 5 to 8 on the gauge section. The S_a values for both materials are between 0.0015 and 0.0036 mm, with S_z values consistently higher for the GA05-25Ni (0.023 to 0.038 mm) than those of the GA05-20Ni (0.013 to 0.018 mm). This also translates to the S_z values with a standard deviation difference in maximum height of around 12 microns between both materials.

No significant increase in S_a and S_z were found between the tab and the gauge sections, indicating a consistent polishing of each sample. The linescan results are consistent with the area mappings, but the direction of the line scan showed a larger impact on the direction of the linescan. This result can be attributed to the polishing direction of the final polishing step; the relief marks shown in Figure 7

highlight the slightly different orientations impacting the R_a and R_z values. An example of the 11 linescans conducted per sample is shown in Figure 9 for the GA05-25Ni samples, with the average height of the R_a and R_z values of the 11 linescans per sample shown on the bottom.

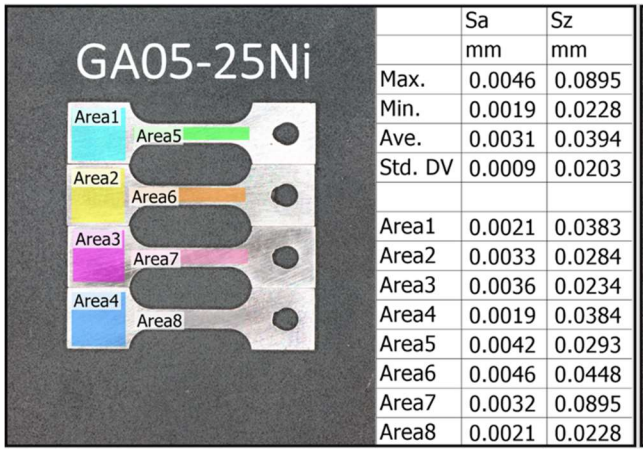

	Sa	Sz
	mm	mm
Max.	0.0046	0.0895
Min.	0.0019	0.0228
Ave.	0.0031	0.0394
Std. DV	0.0009	0.0203
Area1	0.0021	0.0383
Area2	0.0033	0.0284
Area3	0.0036	0.0234
Area4	0.0019	0.0384
Area5	0.0042	0.0293
Area6	0.0046	0.0448
Area7	0.0032	0.0895
Area8	0.0021	0.0228

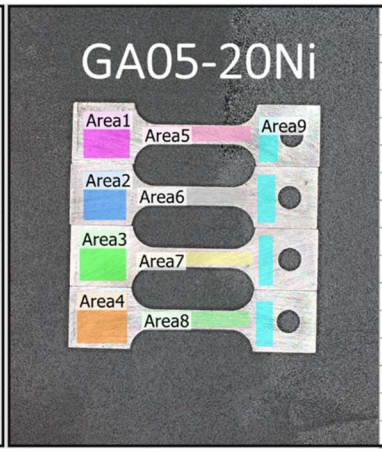

	Sa	Sz
	mm	mm
Max.	0.0065	0.0395
Min.	0.0015	0.0125
Ave.	0.0028	0.0202
Std. DV	0.0015	0.0083
Area1	0.0015	0.0130
Area2	0.0022	0.0125
Area3	0.0030	0.0185
Area4	0.0018	0.0188
Area5	0.0015	0.0395
Area6	0.0029	0.0201
Area7	0.0031	0.0159
Area8	0.0025	0.0145
Area9	0.0065	0.0294

Figure 8. Roughness measurement positions of each area in the comparison between both materials.

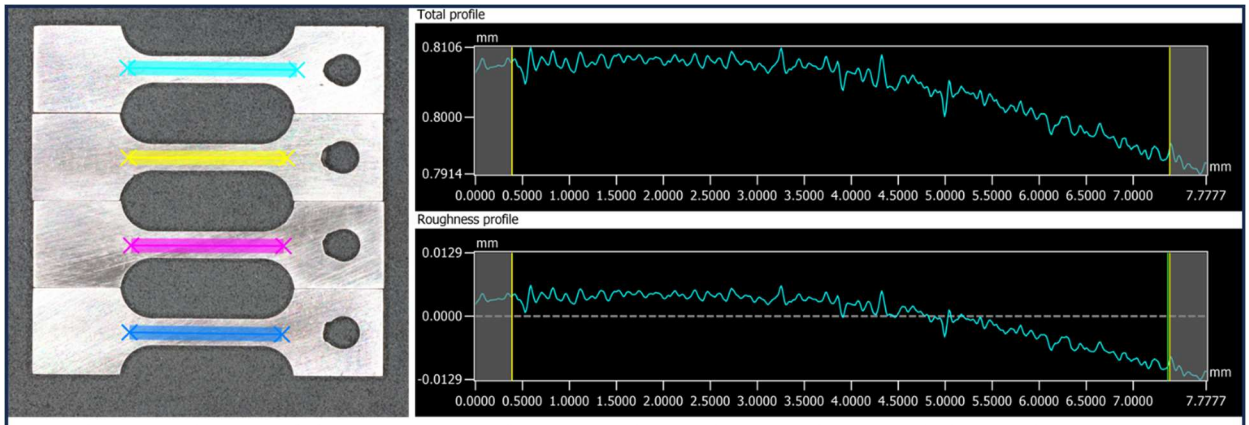

	Ra/Pa/Wa	Rz/Pz/Wz
	mm	mm
Ave.	0.0039	0.0181
Max.	0.0048	0.0206
Min.	0.0030	0.0151
Std. DV	0.0006	0.0016

	Ra/Pa/Wa	Rz/Pz/Wz
	mm	mm
Ave.	0.0041	0.0231
Max.	0.0047	0.0318
Min.	0.0035	0.0183
Std. DV	0.0004	0.0037

	Ra/Pa/Wa	Rz/Pz/Wz
	mm	mm
Ave.	0.0028	0.0139
Max.	0.0034	0.0164
Min.	0.0022	0.0116
Std. DV	0.0004	0.0013

	Ra/Pa/Wa	Rz/Pz/Wz
	mm	mm
Ave.	0.0016	0.0102
Max.	0.0025	0.0122
Min.	0.0008	0.0059
Std. DV	0.0006	0.0018

Figure 9. Linescan example across the gauge section of GA05-25Ni samples.

3. HFIR EXPERIMENT

3.1 HFIR FACILITY

The experiment capsules are being designed for irradiation in HFIR's central flux trap, shown below in Figure 10. The rabbit capsules are designed for loading into tubes called *target rod rabbit holders* (TRRHs) or *peripheral target positions* (PTPs) within in the flux trap. Each of these TRRHs or PTPs has up to eight axial positions with centerlines at axial position 4 for TRRH and axial position 5 for PTP. HFIR's highest steady-state neutron fast flux, 1×10^{15} n/cm^2/s, occurs closest to the fuel in the PTP positions, whereas the highest thermal flux, 2×10^{15} n/cm^2/s, occurs at the centermost TRRH position D4

[2]. HFIR operates nominally six cycles per year and 25 days per cycle at a constant power of 85 MW. Irradiation damage within the flux trap for steels can reach 2 dpa per cycle in optimal positions.

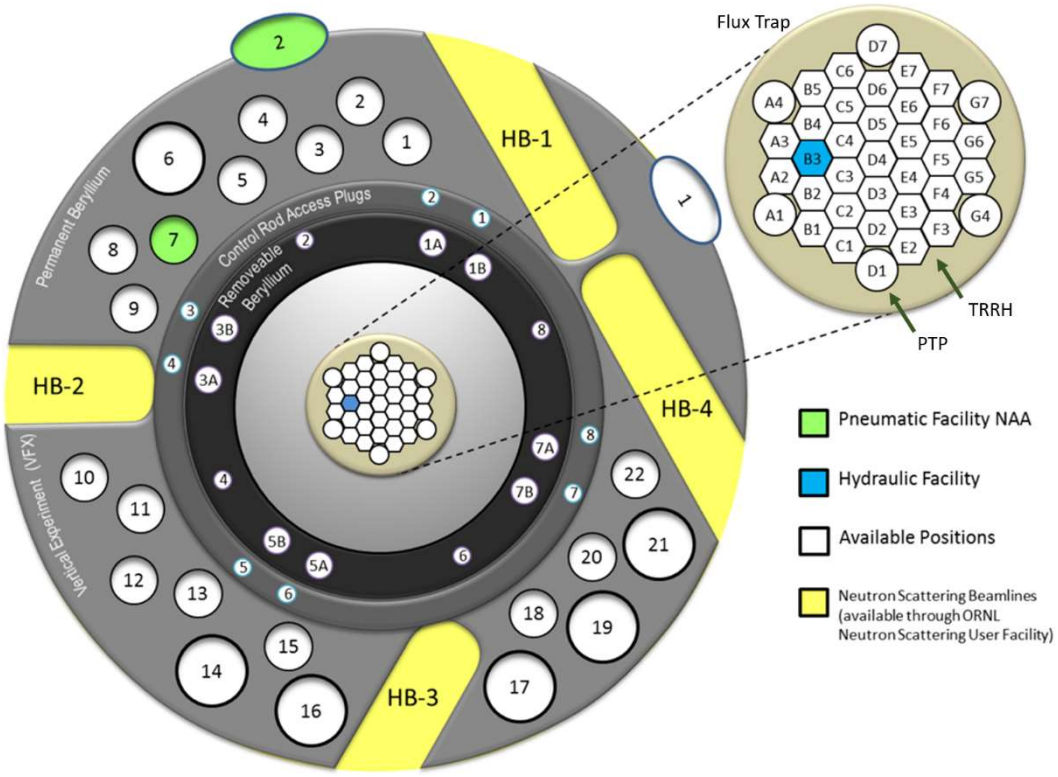

Figure 10. HFIR experiment facilities [2].

3.2 TEST MATRIX

The irradiation test matrix comprises eight irradiation capsules spanning two goal temperatures and the two different Ni compositions discussed previously. The proposed irradiation test matrix is given below in Table 3.

Table 3. Irradiation test matrix

Capsule ID	Irradiation Temperature (°C)	Alloy	Dose (dpa)	# of Cycles
BLR01	400	GA05-20Ni	3	2
BLR02				
BLR03	650			
BLR04				
BLR05	400	GA05-25Ni		
BLR06				
BLR07	650			
BLR08				

3.3 EXPERIMENT DESIGN

The Pb rabbit capsule design is the second iteration of a liquid metal corrosion capsule designed for irradiation in the HFIR flux trap. A set of liquid Sn capsules was irradiated in winter 2022, HFIR cycle 500. These Sn capsules examined corrosion on pre-oxidized oxide dispersion strengthened FeCrAl specimens coupled with neutron irradiation [3]. These Sn capsules demonstrated the safety of liquid metal rabbit capsules in HFIR, as well as the successful recovery of specimens and the accuracy of thermal models. These capsules were filled with solid Sn and designed to melt passively through gamma heating. The Sn was contained within a secondary holder assembly made of Mo. Once the irradiation concluded, the experiment capsules were shipped to an onsite hot cell facility at ORNL for disassembly. During the disassembly, the capsules were inverted, heated to melt the Sn to the opposite end of the capsules, then cut open to retrieve the specimens.

For the liquid Pb experiment, some improvements in the design were implemented, though the main concept for the capsule remains the same. The capsule design is shown in Figure 11 as a CAD representation. Design improvements focus on the accuracy of temperature modeling and simplifying disassembly. The Sn capsule concept described by Kondo et al. [3] included three tensile specimens with two SiC thermometers. However, the final rabbit capsules irradiated in HFIR contained two tensile specimens and one SiC thermometers. This was done to increase the ratio of Sn to specimens. For the liquid Pb capsule experiment, the specimen quantities were increased back to three tensile specimens with two SiC thermometers.

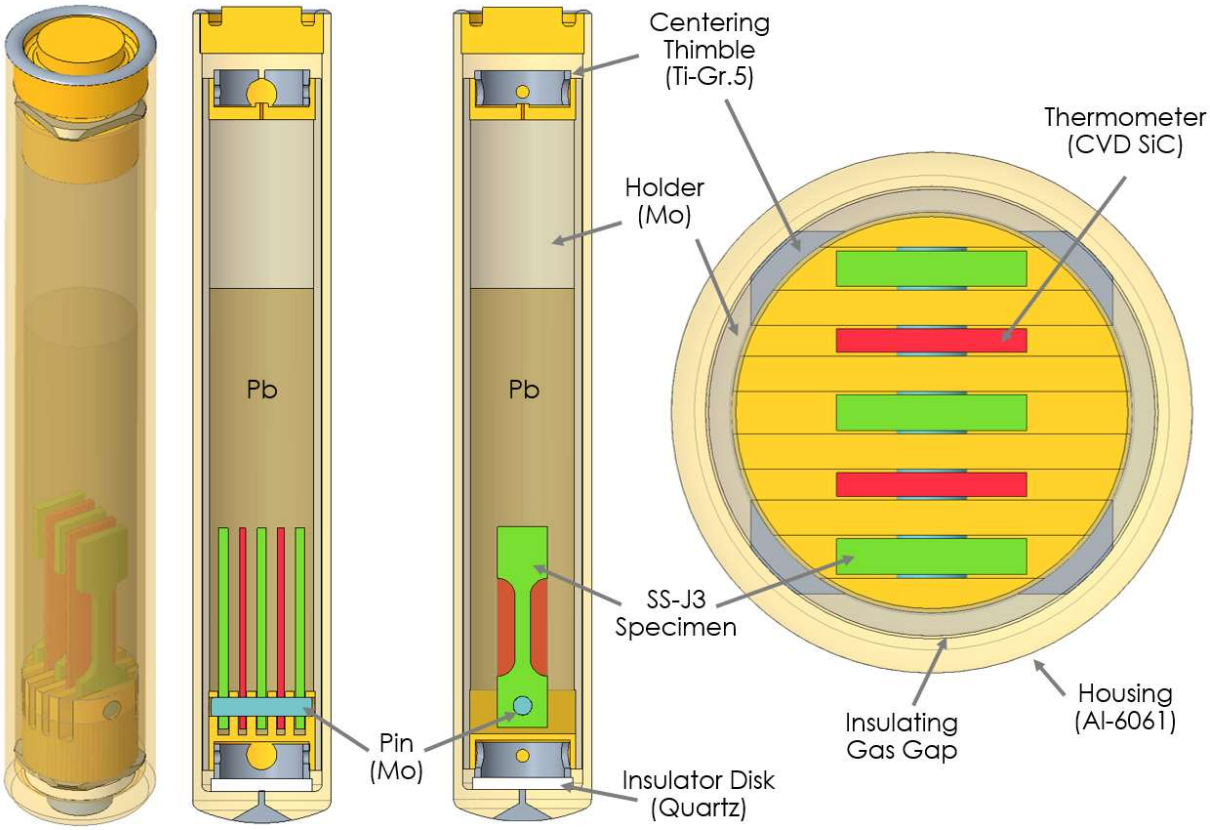

Figure 11. Liquid Pb HFIR experiment.

The experiment houses a seal-welded internal holder made of Mo designed to contain the liquid metal. Conservatism in the holder wall thickness was relaxed from nominally 760 µm to 585 µm. This reduction in Mo allows for an increase in the amount of Pb in the system. Additionally, the decreased wall thickness will ease capsule disassembly. During the hot cell disassembly, a section of the holder is broken off exposing the internal components. The thinner wall will simplify this process. The Mo holder is still sufficiently strong at these operating temperatures to contain the liquid Pb, based on previously performed calculations on Mo containers for use in HFIR.

The experiment design uses centering thimbles to constrain the holder assembly such that it is centered within the Al-6061 rabbit housing. This produces an insulating gas gap between the holder and housing that is optimized for both size (by varying the holder outer diameter) and composition (He/Ar percentage). The optimization of the gas gap is the temperature controlling mechanism for the experiment. In the previous Sn experiment, the holder had machined tabs designed to center the holder included in the part. The machined tabs complicated the fabrication of the holder, reducing machining accuracy. Moving to the centering thimble design aims to simplify fabrication of the holder, increasing the machining accuracy of the holder to control this sensitive dimension, as well as to decrease costs.

The capsule parts were fabricated in accordance with the ORNL Research Reactor Division's quality assurance program. An example set of capsule parts is given below in Figure 12.

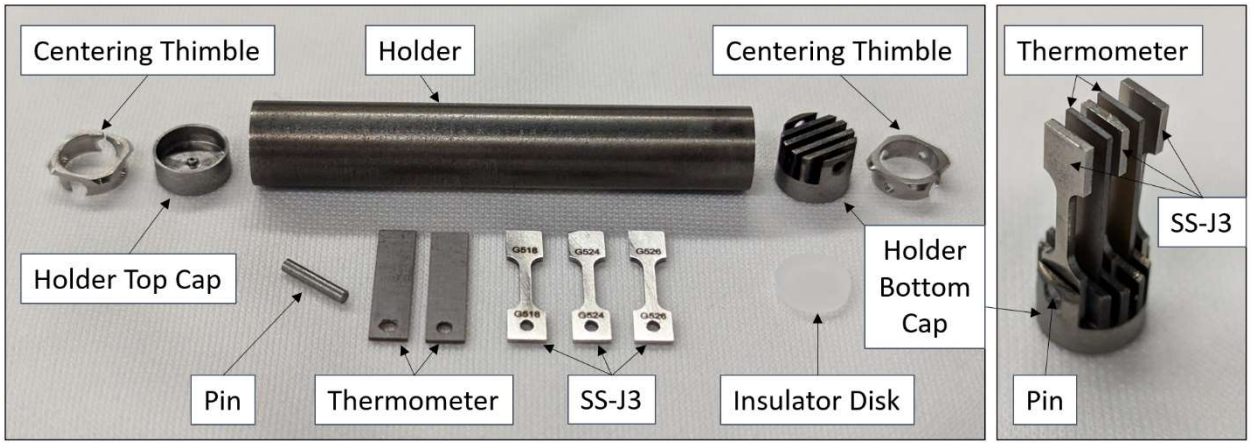

Figure 12. Example of internal capsule components. Aluminum housing not pictured.

3.4 NEUTRONICS ANALYSIS

A neutronics calculation was performed to compute the heat generation rates (HGRs) from neutron and photon irradiation in all the components of the experiment. The computed HGRs contain heating contributions from all irradiation sources and include prompt and delayed heating. Figure 13 shows the HFIR Monte Carlo N-Particle Transport (MCNP) code modeling of the target in the HFIR flux trap. For each of the selected target locations (PTP-A1 and TRRH-B2), the experiment was modeled as part of a rabbit train and with the main experiment capsule located on the core centerline. The rabbit train included three additional empty Al rabbits above the target and four below the target. The purpose of modeling a rabbit train instead of a single experiment suspended in water was to minimize the spatial shielding of the target.

Figure 13(a) shows an X-Z view of the flux trap through the target, and Figure 13(b) shows an X-Y view through the core midplane with the target located in PTP-A1 and TRRH-B2 positions, respectively. Figure 14 shows close-up views of the Pb target.

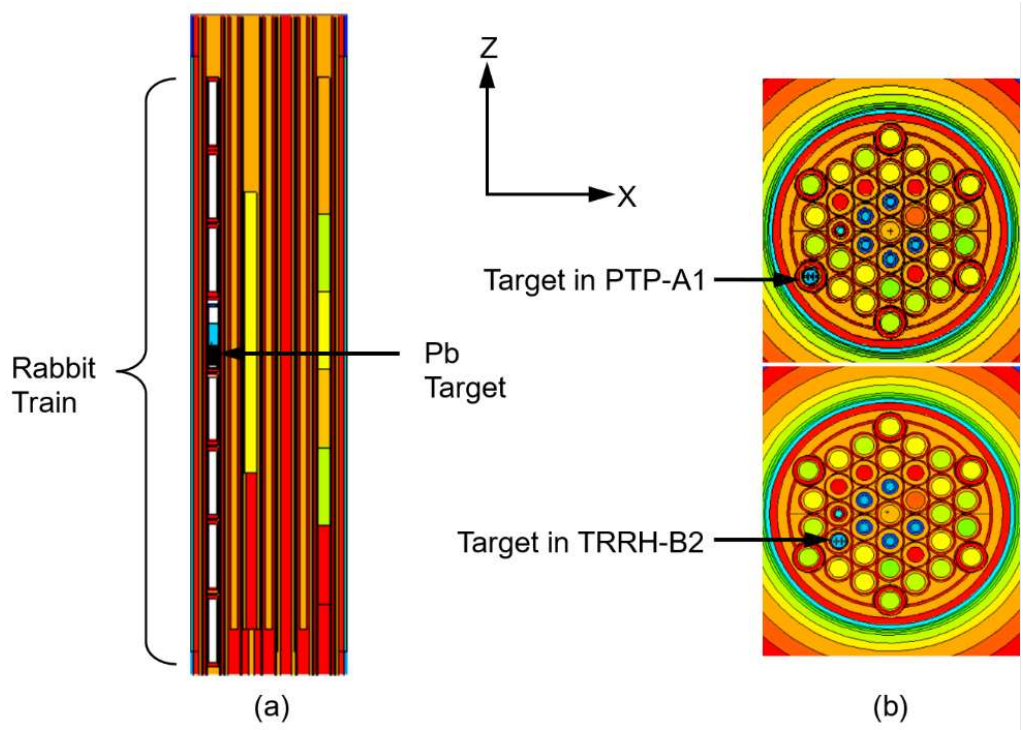

Figure 13. Experiment location in HFIR Flux Trap. (a) X-Z view of rabbit train in position A1; (b) Rabbit inside A1 and B2 positions of the HFIR MCNP model.

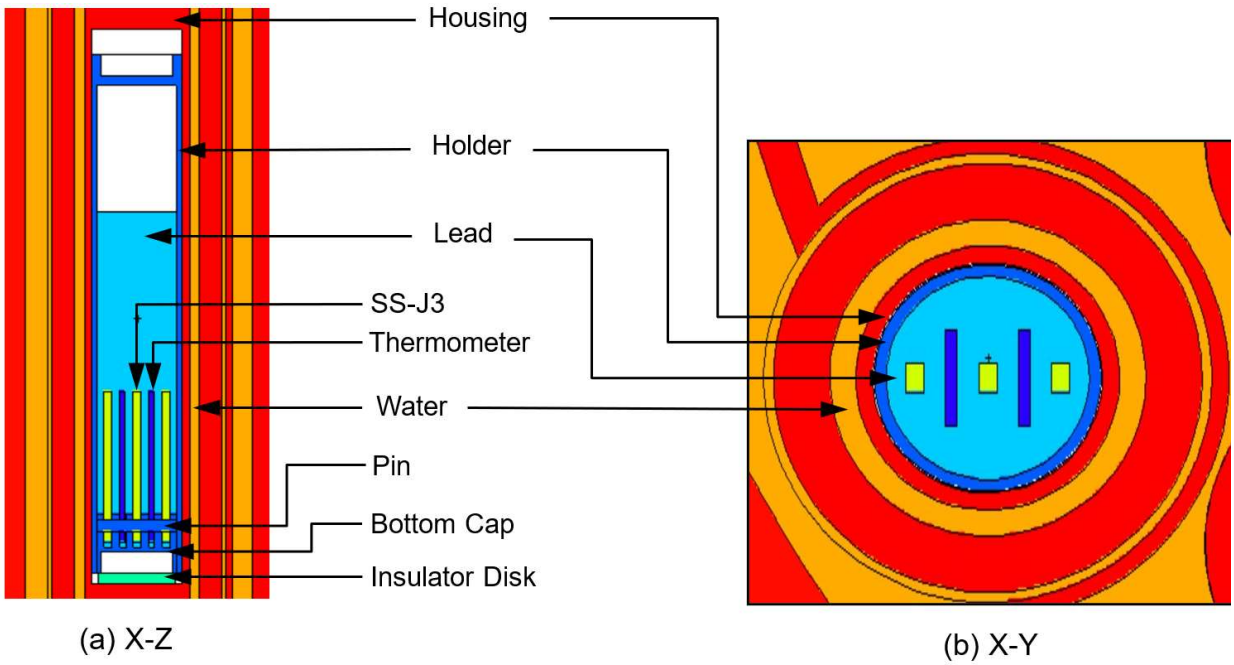

Figure 14. Close up views of Pb target model.

The target was simulated for two HFIR cycles in each of the respective positions. The average component HGRs were calculated as the sum of the average HGR of each heating source. The average HGRs were used in the design thermal analyses reported later in this report. The maximum component HGRs were then calculated as the sum of the maximum HGR of each heating source, followed by adding a 3σ calculation uncertainty. This maximum HGR is used for safety calculations to satisfy HFIR qualification requirements. Table 4 show the HGRs for positions PTP-A1 and TRRH-B2, respectively.

Table 4. Target heating results for position PTP-A1

Component	Initial Mass (g)	Avg. Total Heating (W/g)	Max. Total Heating (W/g)	1s (W/g)	Max. + 3s (W/g)
SS-J3 (1)	0.226	20.97	22.17	0.39	23.33
SS-J3 (2)	0.226	22.94	24.19	0.36	25.26
SS-J3 (3)	0.226	22.23	23.52	0.39	24.69
Thermometer (1)	0.103	22.40	23.08	0.44	24.38
Thermometer (2)	0.103	21.78	22.51	0.33	23.49
Bottom Cap	1.450	35.43	36.20	0.31	37.12
Lead	19.600	47.34	48.35	0.20	48.96
Pin	0.148	31.11	32.69	0.68	34.75
Holder	8.460	40.89	41.62	0.13	42.02
Insulator Disk	0.111	27.64	28.39	0.37	29.51
Housing	5.070	27.13	27.81	0.15	28.26

Table 5. Target heating results for position TRRH-B2

Component	Initial Mass (g)	Avg. Total Heating (W/g)	Max. Total Heating (W/g)	1s (W/g)	Max. + 3s (W/g)
SS-J3 (1)	0.226	20.31	22.11	0.52	23.67
SS-J3 (2)	0.226	22.13	23.58	0.56	25.26
SS-J3 (3)	0.226	21.40	22.70	0.44	24.00
Thermometer (1)	0.103	20.90	21.62	0.40	22.81
Thermometer (2)	0.103	20.75	21.45	0.50	22.96
Bottom Cap	1.450	33.27	34.32	0.43	35.62
Lead	19.600	44.69	45.48	0.25	46.23
Pin	0.148	30.35	33.57	1.28	37.41
Holder	8.460	37.69	38.50	0.18	39.03
Insulator Disk	0.111	26.42	27.79	0.57	29.51
Housing	5.070	25.68	26.33	0.19	26.89

3.5 THERMAL ANALYSIS

The CAD model of the liquid Pb capsule from Figure 11 was imported into the ANSYS finite element software for thermal analysis. The ANSYS model takes advantage of the symmetry present in the capsule by cutting the model into a 90-degree symmetry model. The gamma heating rates determined in Section 3.4 were applied to the internal components of the capsule. A thermal circuit is created such that heat is conducted from internal components through the insulative gas gap, thereby establishing desired specimen temperatures, and is ultimately rejected to the HFIR coolant. This common approach to passively controlling specimen temperature is achieved by varying the insulating gas gap (size and composition) and adjusting the axial position in HFIR.

The ORNL Irradiation Engineering Group manages a database of design and analysis calculations (DACs) that include temperature-dependent thermophysical material properties used in thermal analyses. These DACs are available upon request. A DAC including liquid properties for Pb has not been created;

therefore, the thermophysical properties for liquid Pb used in the thermal analyses were taken from Sobolev [4].

A response surface optimization was performed within ANSYS to determine the combination of variables that (1) achieves the two irradiation temperatures within the specimen gauge region and (2) minimizes the temperature distribution across the specimen gauge region. The response surface model was set up to analyze a range of holder diameters between 9.0 and 9.5 mm and a He fill gas composition with Ar balance. The model used a nominal housing internal diameter of 9.519 mm, resulting in an insulating gas gap range from 10 to 260 µm. The response surface output is given in Figure 15, as an example for the TRRH axial position 2. The ANSYS optimization module then found that peripheral axial positions 1, 2, 6, and 7 have a smaller axial temperature distribution across the length compared to that of central positions 3 through 5. It was also observed that a larger diameter holder will have a smaller axial temperature distribution across the length compared to a smaller holder diameter at the same average specimen temperatures.

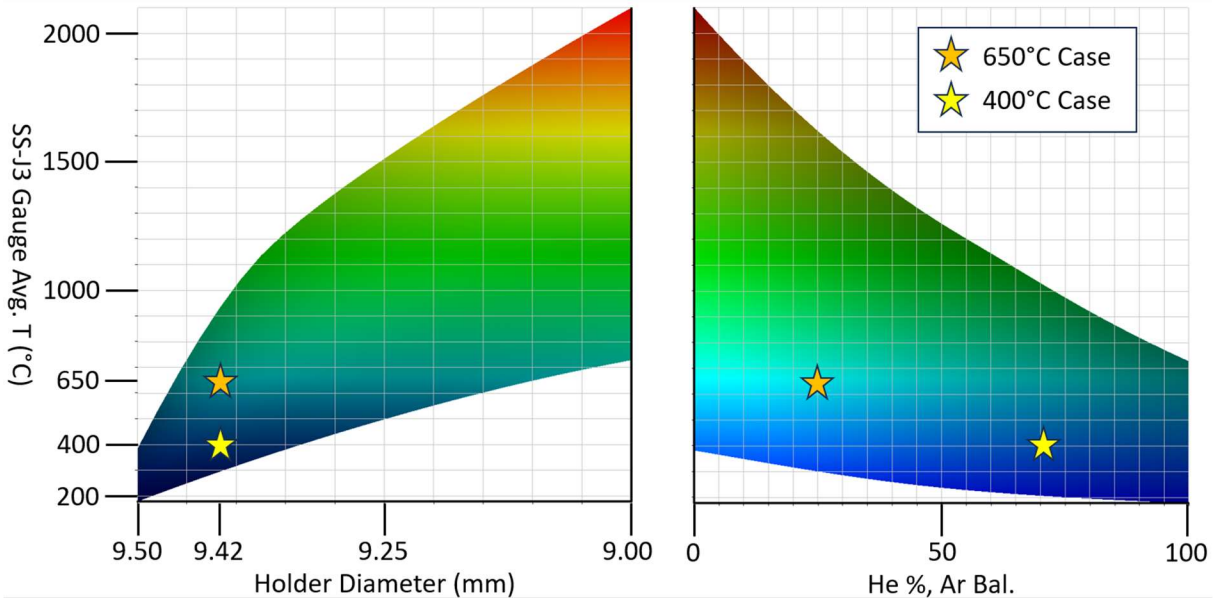

Figure 15. Response surface for TRRH axial position 2.

A 9.42 mm holder diameter was chosen for this experiment because it enabled the ability to hit both desired temperatures with the same part. This reduces fabrication complexity and gives flexibility during the capsule build to move parts around. This is especially important as parts are delivered with machining tolerance variability. The fill gas composition can be altered if needed to correct for the machining variability.

After the response surface optimization was performed, the suggested candidate points were individually verified within the ANSYS model for accuracy. Analyzing the individual cases validates the response surface recommendation and generates temperature contour plots. The predicted component temperatures for the different cases are presented in Table 6. The analyzed cases assume the 9.42 mm holder diameter suggested from the optimization. Due to machining tolerances and space availability in HFIR, the as-built capsules may vary slightly. The gas compositions shown are He with Ar balance. The inner and outer specimens are reported separately. Additionally, the specimens are split along the gauge and tab regions. Averages are reported as volume weighted.

Expected temperature distributions are provided for the 400 °C case in Figure 16 through Figure 19 and for the 650 °C case in Figure 20 through Figure 23. For each temperature case, the specimen temperature distributions are given for both inner and outer specimens, as well as specimen tabs and gauge regions. Temperature distributions are also given for the SiC thermometer. The analyzed temperature measurements for the thermometers will be performed during the post-irradiation examination. Those measurements can be compared to the results presented below.

Table 6. Experiment predicted component temperatures

	Component Temperature [avg (max, min)]			
	Holder Outer Diameter: 9.42 mm			
	400 °C		650 °C	
Component	**TRRH-2 (71% He)**	**PTP-3 (81% He)**	**TRRH-2 (25% He)**	**PTP-3 (32% He)**
Housing	64 (71, 55)	67 (75, 57)	64 (70, 55)	67 (74, 57)
Housing End Cap	73 (75, 71)	74 (76, 72)	94 (95, 91)	94 (96, 92)
Holder	320 (393, 202)	313 (387, 194)	528 (625, 365)	523 (623, 355)
Holder Caps	300 (380, 241)	295 (378, 234)	504 (602, 423)	499 (603, 414)
Centering Thimbles	279 (338, 201)	273 (332, 191)	471 (549, 386)	464 (547, 372)
Lead	413 (486, 305)	411 (491, 298)	632 (703, 507)	634 (711, 501)
Pin	369 (373, 363)	365 (370, 358)	597 (600, 593)	595 (599, 590)
Insulator Disk	127 (263, 71)	128 (261, 74)	184 (398, 87)	185 (403, 88)
Thermometer	411 (459, 356)	411 (462, 352)	630 (678, 580)	633 (683, 578)
SS-J3 (inner, gauge)	430 (447, 391)	433 (450, 391)	646 (664, 609)	650 (669, 611)
SS-J3 (outer, gauge)	389 (413, 346)	386 (412, 341)	611 (636, 568)	611 (638, 565)
SS-J3 (inner, tabs)	415 (466, 362)	418 (470, 358)	635 (684, 586)	638 (690, 584)
SS-J3 (outer, tabs)	381 (430, 342)	359 (430, 336)	606 (655, 563)	605 (657, 560)
SS-J3 (combined, gauge)	403 (447, 346)	402 (450, 341)	622 (664, 568)	624 (669, 565)

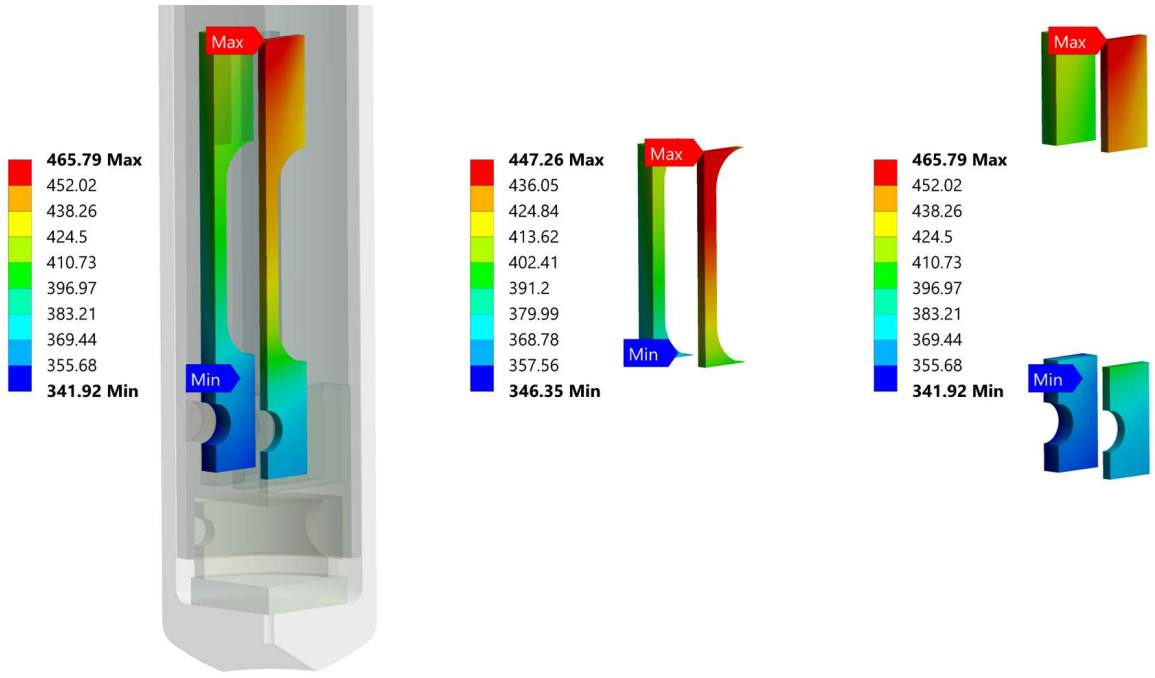

Figure 16. SS-J3 specimen temperature distribution (400 °C, TRRH-2).

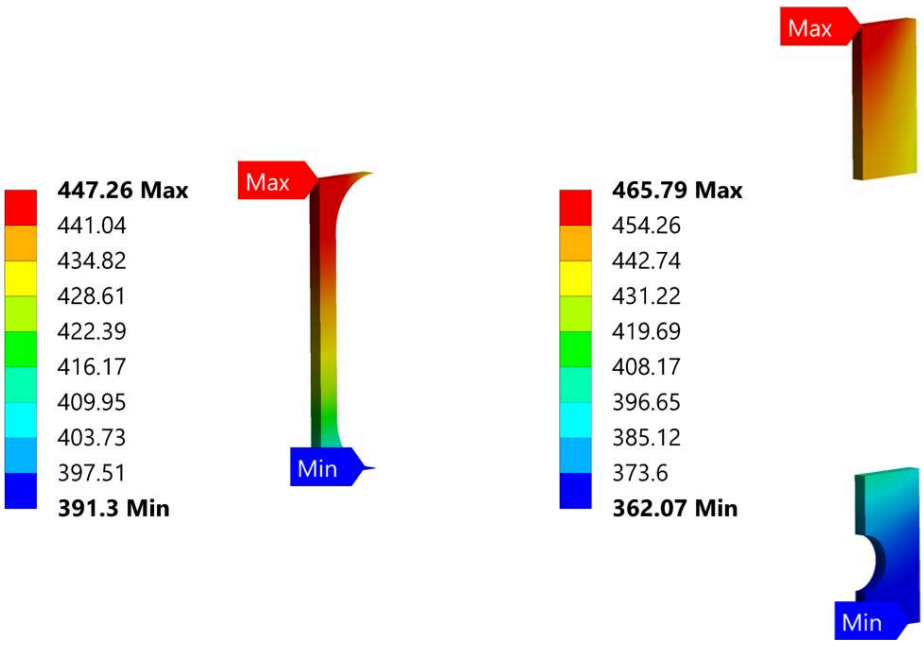

Figure 17. Inner SS-J3 specimen temperature distribution (400 °C, TRRH-2).

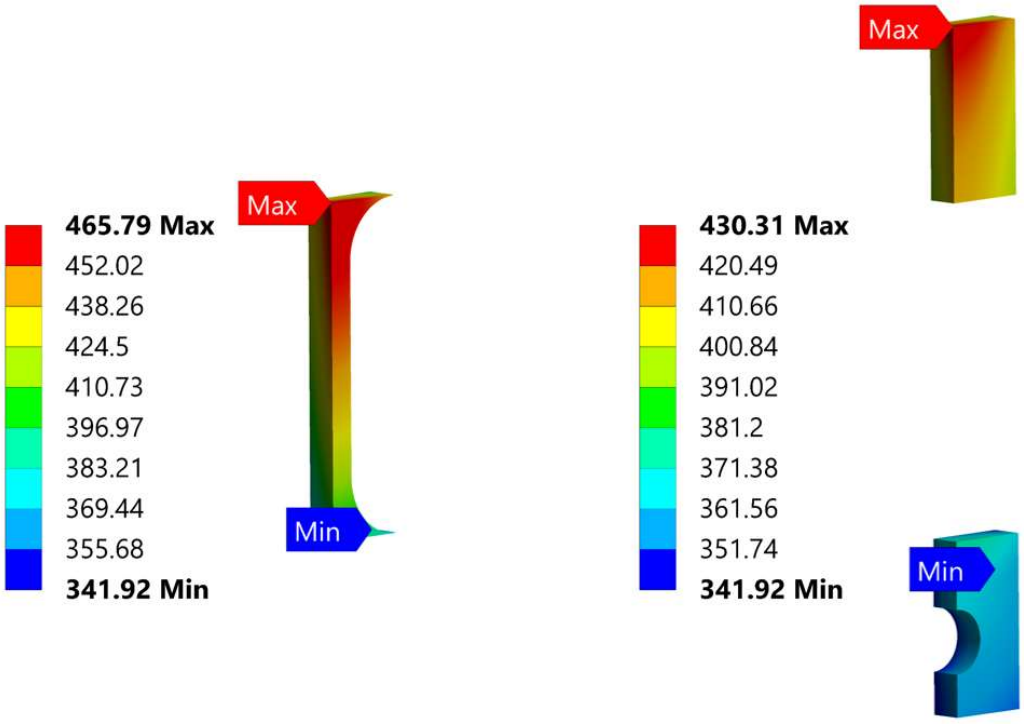

Figure 18. Outer SS-J3 specimen temperature distribution (400 °C, TRRH-2).

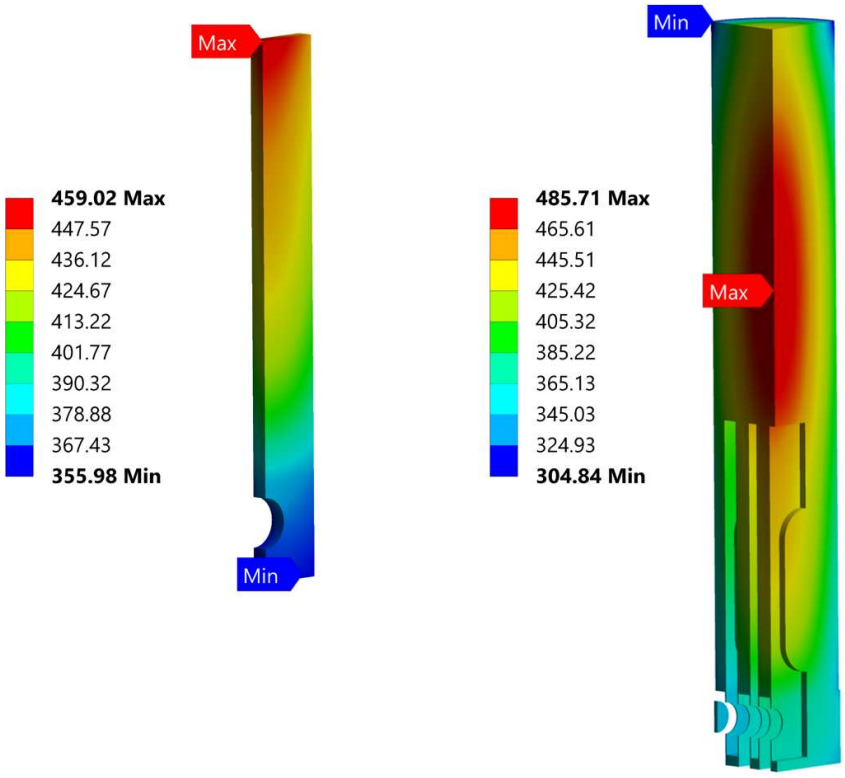

Figure 19. SiC thermometer (left) and Pb (right) temperature distribution (400 °C, TRRH-2).

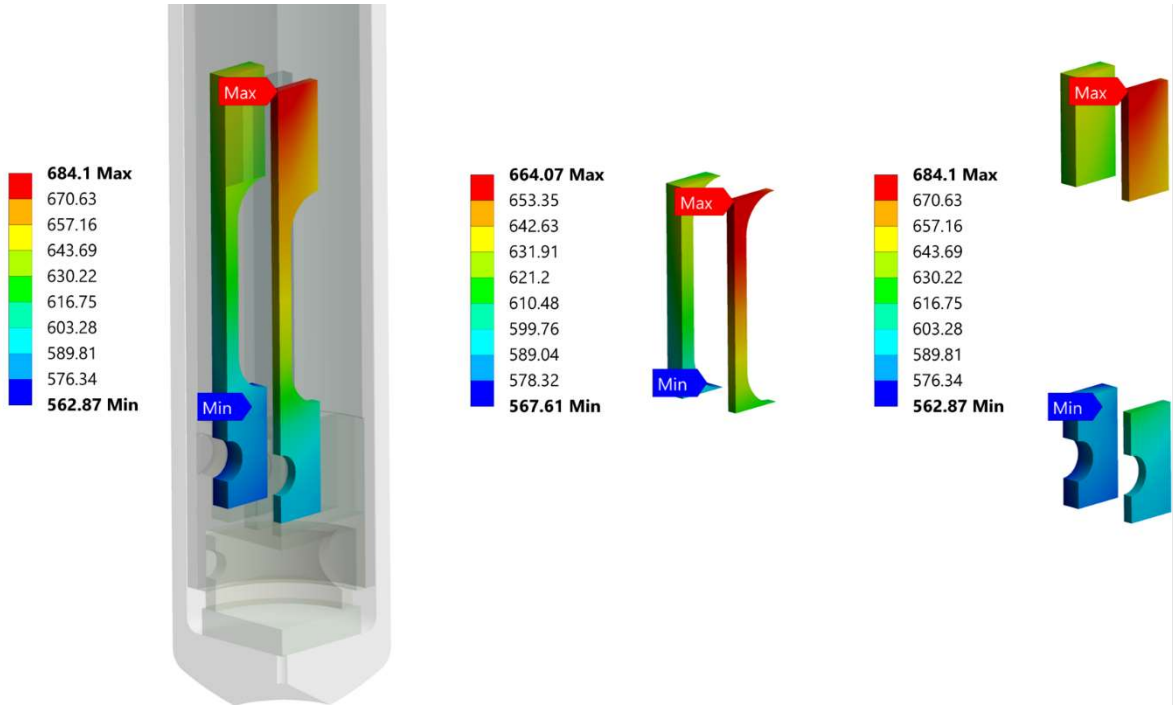

Figure 20. SS-J3 specimen temperature distribution (650 °C, TRRH-2).

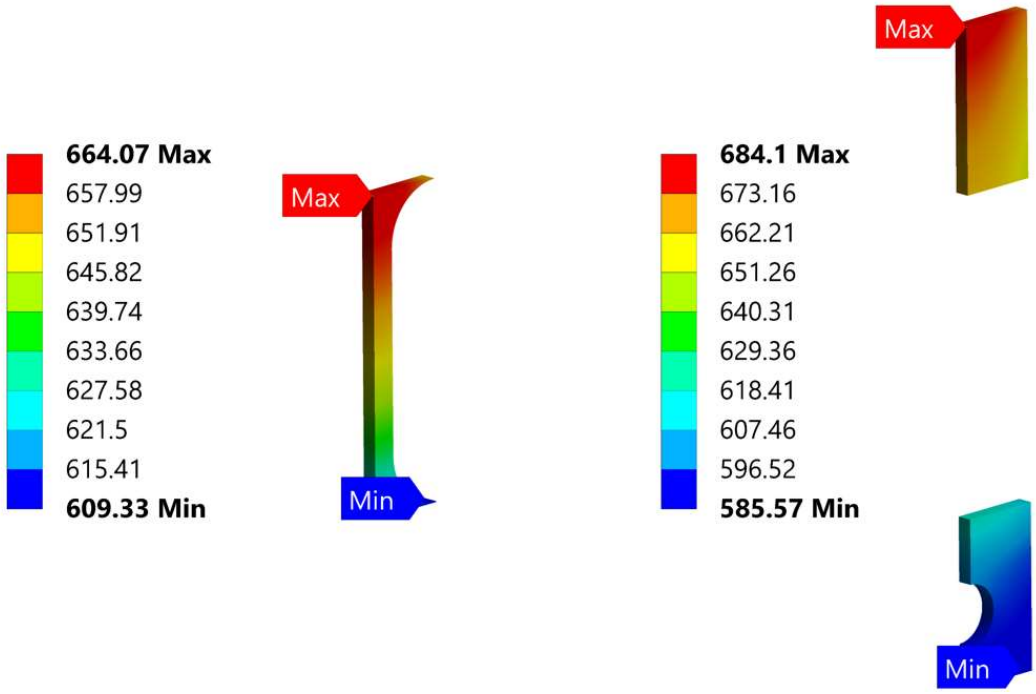

Figure 21. Inner SS-J3 specimen temperature distribution (650 °C, TRRH-2).

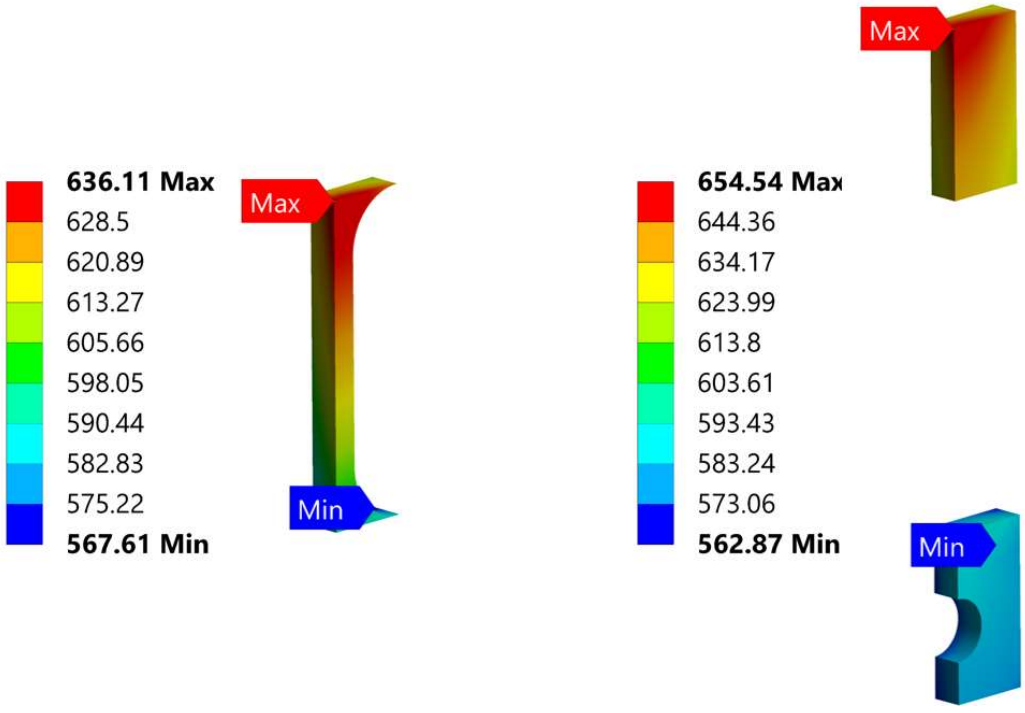

Figure 22. Outer SS-J3 specimen temperature distribution (650 °C, TRRH-2).

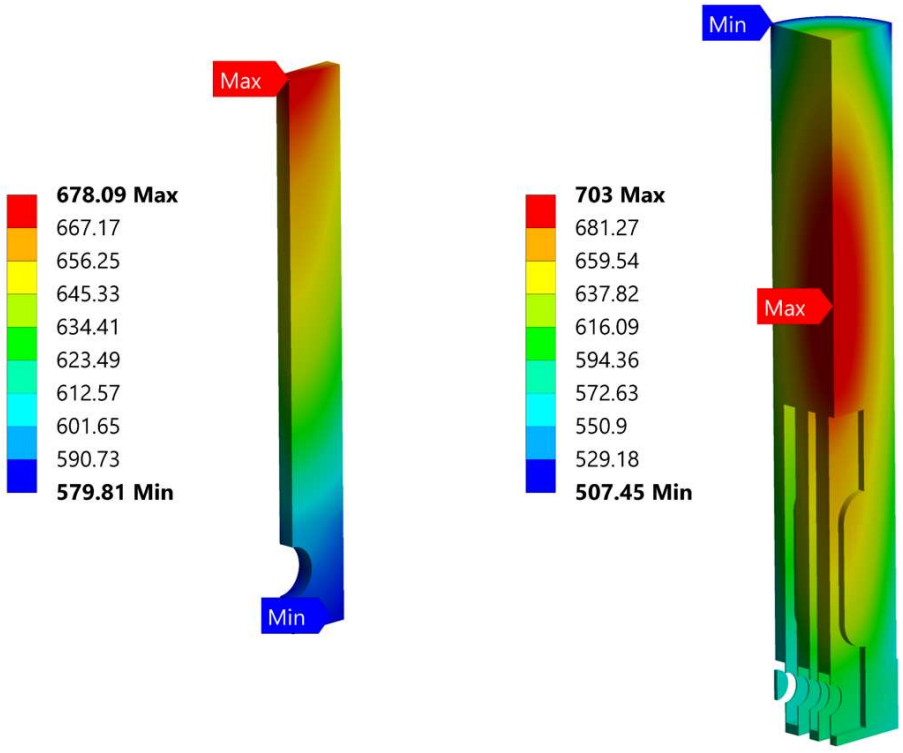

Figure 23. SiC thermometer (left) and Pb (right) temperature distribution (650 °C, TRRH-2).

4. CONCLUSIONS

To evaluate the susceptibility of AFA stainless steels to liquid metal embrittlement under coupled effects of neutron irradiation and corrosion, an irradiation experiment has been designed. This experiment utilizes the gamma heating with the HFIR flux trap to melt Pb within the capsules. The Pb is allowed to interact with the AFA steels and accumulate damage up to the goal of 3 dpa. The experiment capsules will be allowed to solidify and will then be shipped to an onsite hot cell facility for disassembly and specimen recovery. The specimens will then undergo miniature tensile testing, microscopy, mass spectroscopy, and sectioning. The specimens have been fabricated from two different AFA alloys, GA05-25Ni and GA05-20Ni, with differing Ni content. In addition, the thermal design for the experiment has been established with a combination of neutronics and finite element thermal analyses. The capsules are scheduled to be assembled and irradiated in calendar year 2025.

5. REFERENCES

[1] B. A. Pint, Y. Su, M. P. Brady, Y. Yamamoto, J. Jun and M. R. Ickes, "Compatibility of Alumina-Forming Austenitic Steels in Static and Flowing Pb," *JOM,* vol. 73, no. 12, pp. 4016-4022, 2021.

[2] Oak Ridge National Laboratory, *HFIR Flux Isotope Reactor (HFIR) User Guide - A guide to in-vessel irradiations and experiments,* Revision 2.0, 2015.

[3] M. Kondo, B. A. Pint, J. Jun, N. G. Russell, J. L. McDuffee, M. Akiyoshi, T. Tanaka, N. Oono, J. Miyazawa, J. W. Geringer, Y. Katoh and Y. Hatano, "Conceptual Design of HFIR Irradiation Experiment for Material Compatibility Study on Liquid Sn Divertor," *Plasma Fusion Res.,* vol. 16, no. 2405040, 2021.

[4] V. Sobolev, "Database of thermophysical properties of liquid metal coolants for GEN-IV," SCK/CEN, Mol, Belgium, 2011.